# Enhancing efficiency of field assisted sintering by advanced thermal insulation

Alexander M. Laptev[a,*], Martin Bram[a], Kim Vanmeensel[b], Jesus Gonzalez-Julian[a], Olivier Guillon[a]

[a] Institute of Energy and Climate Research - Materials Synthesis and Processing (IEK-1),

Forschungszentrum Jülich GmbH,

52425 Jülich, Germany

Laptev@gmx.net, m.bram@fz-juelich.de, j.gonzalez@fz-juelich.de, o.guillon@fz-juelich.de

[b] Department of Materials Engineering, Katholieke Universiteit Leuven,

Kasteelpark Arenberg 44, B-3001 Heverlee, Belgium

Kim.Vanmeensel@kuleuven.be

* Corresponding author. E-mail address: laptev@gmx.net (A. M. Laptev)

**Declaration of interest: none.**

# Abstract

The influence of advanced thermal insulation on energy consumption and temperature distribution during electric field assisted sintering of conductive stainless steel powder and non-conductive zirconia powder was investigated. Four types of tool setup were considered: i) without insulation, ii) with die wall insulation, iii) with additional insulation of die faces and iv) with spacers manufactured from carbon fiber reinforced carbon composite (CFRC). The influence of thermal insulation on energy consumption was experimentally studied for samples with diameter of 17 mm. The temperature distribution in samples with diameters of 17 mm, 50 mm and 150 mm was modeled using the Finite Element Method. The power consumed during dwell was almost half the value when die wall insulation was used. The additional insulation of die faces and the application of CFRC spacers provide a threefold decrease in power during sintering of steel powder and a fivefold reduction during sintering of zirconia powder. The advanced thermal insulation significantly homogenizes the temperature distribution within samples of small and medium size. The advanced thermal insulation provides a strong decrease in the temperature gradient inside large conductive sample with a diameter of 150 mm. However, insulation apparently cannot ensure acceptable temperature homogeneity within non-conductive parts of such diameter. The reason for this is the specific current path and related heat concentration near the sample edge.



*Keywords*: Field assisted sintering; Thermal insulation; Energy consumption; Finite element modeling; Temperature distribution

# 1. Introduction

Field Assisted Sintering Technique (FAST), also known as Spark Plasma Sintering (SPS), is a sintering technology based on resistive heating to consolidate powders in an electrically conductive die. Sintering during FAST/SPS is additionally supported by uniaxial pressure. This specific configuration allows densification of ceramic and metallic powders with a tailored microstructure at a high heating rate and with a short processing time. The direct contact between the FAST/SPS tool and water-cooled metallic electrodes provides rapid and/or controlled cooling of sintered samples. Easy sample preparation, flexibility in sintering parameters, short sintering cycle and the availability of highly sophisticated equipment explains the popularity of the FAST/SPS technique within the scientific community. Nowadays, this technique is successfully used in many laboratories worldwide to sinter metals, alloys, ceramics, composites, functionally graded and other advanced materials. Commonly, sintered samples are small in size (10-20 mm in diameter) and only a few sintering cycles a day are performed. Therefore, matters such as energy consumption, productivity and sintering homogeneity are hardly discussed in the literature. However, these issues become important when the industrial application of this technology is considered in line with its actual development trend. Recently, unique FAST/SPS facilities for sintering of components with diameters of up to 500 mm were manufactured and installed. Automatized lines were developed and put into operation. Further up-scaling and commercialization of the FAST/SPS process requires a critical analysis of energy consumption and the development of new measures for its reduction. In addition, sintering inhomogeneity associated with temperature distribution must be investigated for parts of different sizes, and approaches to reducing it must be developed.

A typical FAST/SPS tool setup consists of cylindrical die, two punches and spacers contacting with water-cooled metallic electrodes (Fig. 1).

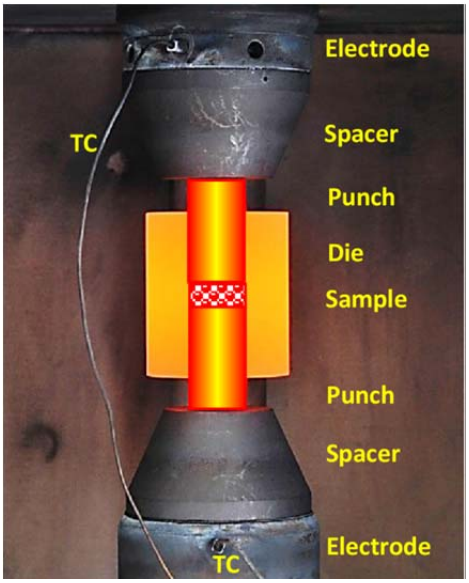


**Fig. 1.** Components of FAST/SPS tool setup and two thermocouples (TC) for measurement of electrodes temperature.

All tool elements (die, punches and spacers) are usually manufactured from a high-strength, isostatically pressed graphite. The initial powder is separated from the die and punches by a graphite foil. This foil improves the thermo-electrical contact between the powder and the tool, and protects them from sticking to each other. The Joule's heat is generated as a consequence of current flow throughout all electrically conductive components. The heat is redistributed within the setup owing to thermal conduction. Some part of the heat is lost due to radiation from the external setup surface. Another portion of heat is lost because of the water cooling of electrodes. Such a setup can be considered an open thermal system with internal heat sources. The corresponding thermal balance can be formulated as $W_j = W_h + W_r + W_c$ , where $W_j$ is the Joule's heat generated due to current flow; $W_h$ is the heat consumed during powder and tool heating-up; $W_r$ is the heat loss due to radiation and $W_c$ is the heat loss due to electrodes cooling. In an energetically effective system, the $W_r$ and $W_c$ components should be minimized. Obviously, thermal insulation of the tool from the electrodes as well as from the ambient reduces the energy consumption during sintering.

There are only a few publications discussing the thermal balance in the FAST/SPS setup. Zavaliangos et al. (2004) reported a radiation-related contribution to a total heat loss ranging from 20% at a temperature of 350°C to 60% at a temperature of 1350°C. Vanmeensel et al. (2007) were

probably among the first to notice the importance of die thermal insulation to reduce radiation energy loss ($W_r$). Nowadays, thermal insulation of the die wall with graphite felt is widely employed in FAST/SPS practice. Nevertheless, the influence of insulation design on energy consumption remains hardly explored. Several solutions for decreasing the heat flow from the FAST/SPS tool towards the water-cooled electrodes ($W_c$) have been proposed. Giuntini et al. (2013) firstly suggested the use of several spacers aiming to reduce the temperature difference between the punch and the electrodes. Then, Giuntini et al. (2015) proposed a new design for punches with drilled cylindrical or machined ring-shaped holes. This design provides a certain reduction in the contact area between the punches and spacers and consequently some decrease in the heat flow towards the electrodes. However, the energy balance has been not discussed. Huang et al. (2017) also decreased the contact area between the punches and electrodes. They proposed a terraced punch design with the part contacting to the spacer having a smaller diameter than the part inserted in the die. Electric current and power input were reduced to 75-85% of their original values for sintering of alumina (1250°C) and copper (850°C). However, the reduced punch cross-section leads to overheating of its narrow part and to a decrease in the maximal admissive load. In the present paper, we discuss two solutions to reduce power and energy required for FAST/SPS. Firstly, we consider the use of thermal insulation not only of the cylindrical die surface but also of its top and bottom faces. Secondly, we propose replacing graphite spacers with spacers manufactured from carbon fiber reinforced carbon composite (CFRC). This composite combines acceptable electrical resistivity with low thermal conductivity. This part of the work was performed experimentally. Another part of our work was dedicated to the influence of thermal insulation on temperature homogeneity in FAST/SPS setups and in samples with different conductivity and with different size. The inhomogeneous temperature distribution can lead to poor densification and unacceptable mechanical and other properties in low temperature areas. At the same time, the overheating can result in undesirable grain growth and even in local melting of material. The tolerable value of temperature difference depends on particular material and requirements to product quality. In

present paper we considered the acceptable temperature difference of 20°C. This number can be revised depending on particular requirements an application. Anyway, the temperature gradients should be minimized as much as possible. The aim of our work was to give an inside into the possibilities and limitations of thermal insulation for reduction in temperature inhomogeneity during FAST/SPS sintering. This effect is known but has been scarcely discussed in the literature. Vanmeensel et al. (2007) studied the influence of thermal insulation on temperature distribution in the electrically conductive $ZrO_2$-TiN (60/40) sample with a diameter of 40 mm using the Finite Element Method (FEM). Insulating the die wall with graphite felt resulted in a decreased temperature difference between the center and edge from 147°C to 32°C during dwell at 1500°C. This result was experimentally confirmed by a lower hardness gradient when the sample was sintered in the insulated die. In some cases, thermal insulation can lead to a certain increase in the radial thermal gradient during sintering of non-conductive materials. Achenani et al. (2017) reported this phenomenon for FAST/SPS sintering of alumina at 1300°C in a die with a diameter of 40 mm.

Another possibility to reduce thermal gradients involves optimizing the setup design. Vanherck et al. (2015) used FEM to study the influence of tool geometry on temperature distribution in alumina samples with diameters of up to 60 mm. They found that the radial thermal gradient in non-conductive samples can be significantly reduced by optimizing die wall thickness. Giuntini et al. (2015) proposed the special punch design with drillings or ring-shaped holes, which can influence the current path and temperature distribution within samples. The punch geometry optimized by FEM provided acceptable temperature gradients in a $Si_3N_4$ sample with a diameter of 62 mm. However, drillings and holes led to a decrease in the mechanical strength of punches and to a reduced permissible load.

In the present paper, we systematically examined the influence of conventional and proposed methods of thermal insulation on the temperature distribution in electrically conductive steel (SS316L) samples and non-conductive zirconia (8YSZ) samples. The diameter of the samples was

varied from 17 mm to 150 mm. Thus, the influence of sample conductivity and size on temperature distribution was investigated and explained in-depth. This part of the work was done mainly by Finite Element Analysis.

## 2. Experimental procedures

Two powders with different electrical conductivities were used. The conductive 316L steel powder with particle sizes of 10–36 μm was manufactured by gas atomization at Sandvik Osprey Ltd, UK. Particles of this powder are spherical in shape, and the melting structure can be seen on their surface (Fig. 2a,b). The non-conductive TZ-8Y (8YSZ) zirconia powder with a specific area of 16±3 $m^2$/g was supplied by Tosoh Corp., Japan. Its nano-sized particles are agglomerated into spheres with diameters of several micrometers (Fig. 2c,d).

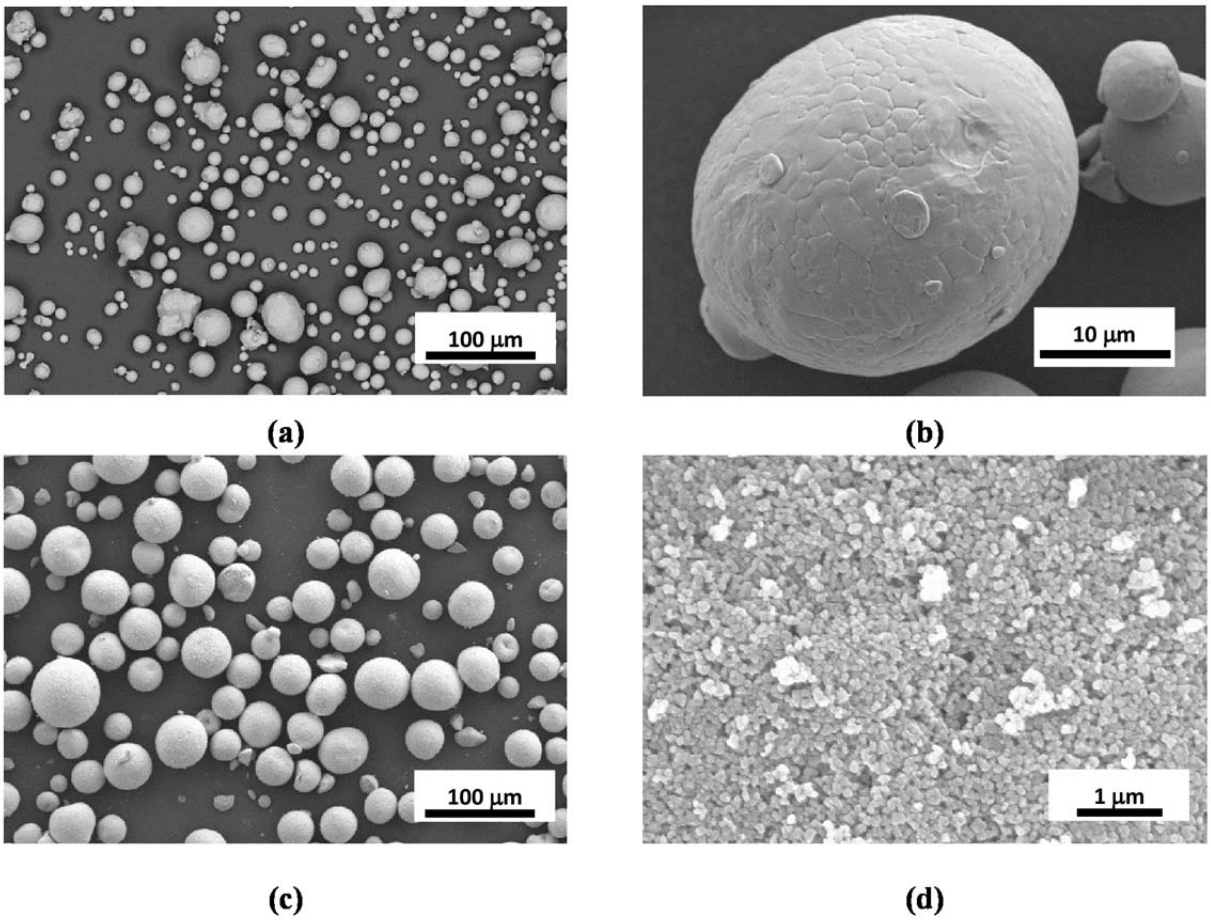


**Fig. 2.** Particles of 316L powder (a), agglomerates of 8YSZ particles (c) and their surfaces (b, d).

Sintering was performed in a HP D 5/2 facility manufactured at FCT Systeme GmbH, Germany. This machine is equipped with a 50 kN uniaxial hydraulic press and with a 37 kW power source.

All experiments were performed in a medium vacuum of 0.6 hPa. The pulsed DC current with 25 ms pulse and 5 ms pause pattern was used for heating. The temperature was measured using a Pyrospot DG 10 N pyrometer (DIAS Infrared GmbH, Germany) near to the sample's top, as described in detail below. The pyrometer's signal was used to generate a preset temperature profile with the PID controller adjusting the supplied power. The four tool setups used in the experiments are shown in Fig. 3. All setups include an identical die, two punches and two spacers.

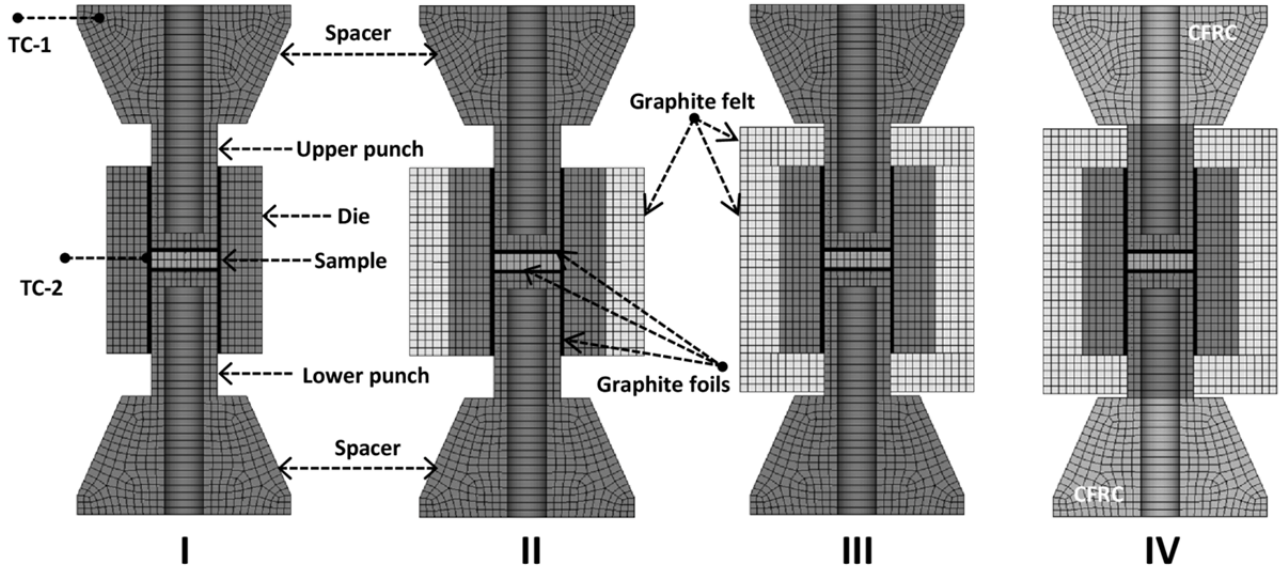


**Fig. 3.** Four setups used in the experiments. The location of additional thermocouples is specified by TC-1 and TC-2.

The cylindrical die with an internal diameter of 17.7 mm, wall thickness of 11.5 mm and height of 48 mm was turned from an isostatically pressed SIGRAFINE® R 7710 fine-grain graphite bar supplied by SGL Carbon GmbH, Germany. The same graphite grade was used to manufacture conical spacers (small diameter of 32 mm, large diameter of 57 mm and height of 30.5 mm) and two punches (diameter of 17 mm, length of 35 mm). Holes with a diameter of 10 mm were drilled in both spacers and punches. The upper blind hole was used to measure the temperature with the pyrometer focused on its bottom at the distance of 4 mm from the sample top. The lower hole was used to affix the setup on the lower electrode. The SIGRAFLEX® graphite foil, grade E (SGL Carbon GmbH, Germany) with a thickness of 0.35 mm was placed between the punches and the die to enhance electrical and thermal conductivity of the contacts and to protect the die wall from

sticking to the powder. The first setup (setup I) included only those components mentioned above. In the second setup (setup II), the external die wall was thermally insulated with SIGRATHERM® soft graphite felt grade GFA 10 (SGL Carbon GmbH, Germany) with a thickness of 11.5 mm. In the setup III, both the top and bottom die faces were additionally insulated with the same felt. The large part of both punches was accordingly co-insulated in this setup. In the fourth setup (setup IV), graphite spacers were replaced by spacers manufactured from SIGRABOND® Premium CFRC composite (SGL Carbon GmbH, Germany). In this case, the die was fully insulated with graphite felt as in the setup III. During experiments with the first, second and third setup, the temperature near the top face of the upper spacer was measured by the K-type thermocouple TC-1 positioned as shown in Fig. 3. In setup I another thermocouple TC-2 was inserted in the die wall. The temperature measured by this thermocouple was used tor validation of FEM model. The temperature in both electrodes near to their contact with the spacers has been also measured (Fig. 1).

The lower punch and the disc punched from graphite foil were first inserted into the die. Then, 7.5 g of 316L powder or 5.5 g of 8YSZ powder were poured. Another graphite foil and the upper punch were placed on the powder column. Afterwards, the powders were pre-compacted in a hand press with a pressure of 50 MPa. FAST/SPS cycles were developed based on preliminary experiments with both powders. These cycles provided sintering of nearly-dense (relative density of above 94%) and crack-free samples. Each cycle included six segments, as shown in Fig. 4: i) pressing with 3 kN force, ensuring safe electrical contact between setup components; ii) heating-up to 450°C, which is the onset temperature of the pyrometer reading; iii) subsequent heating at the rate of 100°C/min to 1050°C for the 316L powder and to 1325°C for the 8YSZ powder; during this stage, the load was simultaneously increased to the maximal value of 11.3 kN (working pressure of 50 MPa); iv) heating at the lower rate of 50°C/min to 1100°C for the 316L powder and to 1375°C for the 8YSZ powder to reduce the temperature overshoot during alteration to dwell; v) holding at maximal temperature and pressure for 5 min for the 316L powder and 30 min for the 8YSZ powder; vi) swift decrease in load to the value of 3 kN and subsequent fast cooling to room temperature. With the

aim of excluding thermal expansion and elastic deformation in the density calculation, a similar cycle with already sintered samples was carried out. The sample temperature, power, current, voltage, lower punch displacement and electrodes temperature were continuously recorded. After sintering, samples were ejected from the die. The graphite foil attached to their surfaces was removed by grinding. All sintered samples had a height of approx. 4 mm. The relative density of sintered samples was measured by the Archimedes' method.

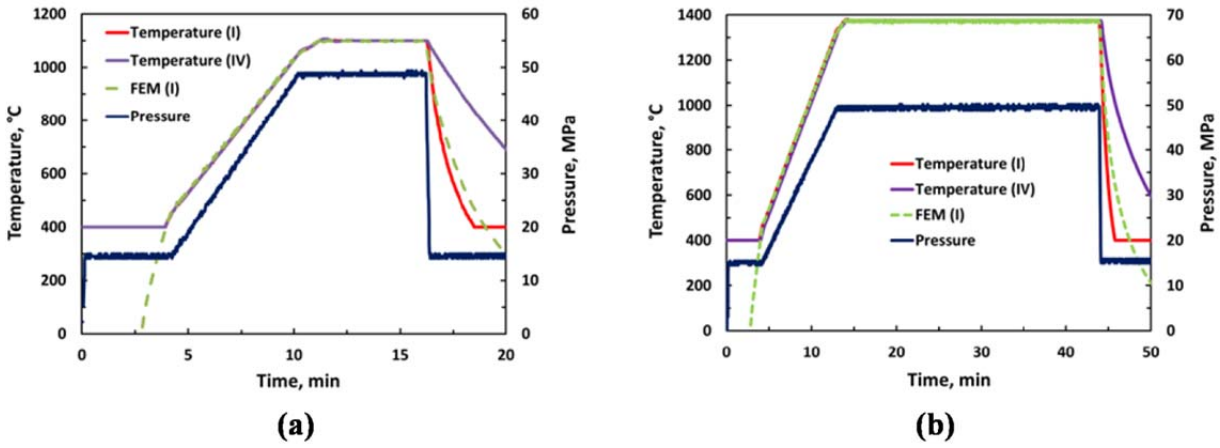


**Fig. 4.** Experimental sintering cycle and temperature profile generated by the virtual controller (FEM) for the 316L powder (a) and 8YSZ powder (b). Numbers in brackets denote setup type.

# 3. Modeling methodology

*3.1. Physical background*

The aim of modeling was to evaluate the impact of thermal insulation on the temperature distribution in FAST/SPS setups, and particularly in samples of different sizes. Modeling of Field Assisted Sintering is usually considered as a solution of an electric-thermal-mechanical problem. The mechanical part of this problem is addressed to punch displacement and associated powder densification. As part of the present research, we studied temperature distributions during the sintering dwell, when powder densification is completed. Thus, in the present study, modeling was reduced to the electric-thermal analysis. The parameters of sintering cycles were taken from the experiments described above. The electric field was modeled using Ohm's and Kirchhoff's laws. The heat generation within the setup components and electrically conductive powder was calculated

using Joule's law. The heat transfer within the system was defined by Fourier's law. The radiation heat loss was evaluated using the Stefan-Boltzmann law. The interaction between spacers and water-cooled electrodes was modeled as convection. In addition, electric and thermal contact resistances were included in the model. Vanmeensel et al. (2005) describe this model in more detail elsewhere.

*3.2. Geometry*

The geometry of the setup was determined by the internal die diameter. Sintering in graphite dies with internal diameters of 17.7 mm, 50.7 mm and 150.7 mm was modeled (Table 1).

**Table 1**

Parameters of dies used during FEM modeling.

| *Internal diameter, mm* | *Wall thickness, mm* | *Height, mm* | *Setup type* |
|---|---|---|---|
| 17.7 | 11.5 | 48 | I-IV |
| 50.7 | 17.5 | 48 | I-IV |
| 150.7 | 20 | 48 | I-IV for 316L<br>IV for 8YSZ |

The die with a diameter of 17.7 mm and other setup elements were geometrically identical to those used in the experiments. This die will be referred as the small-sized die. All four cases of insulation were studied for this die. The influence of sample size on temperature homogeneity was further investigated for the die with an internal diameter of 50.7 mm. This die will be denoted as the medium-sized die. Preliminary FEM analysis showed a strong influence of die wall thickness on temperature distribution in samples sintered in the medium-sized die. We found that the wall thickness of 17.5 mm provides acceptable temperature homogeneity. Diameters of punches and spacers were fitted to this diameter. The height of all setup components was the same as in the small-sized die. All cases of insulation were studied. The largest die (large-sized die) had an internal diameter of 150.7 mm. The die wall thickness of 20 mm was used. Diameters of other setup elements were adjusted to the die diameter. The height of all components was the same as that used in other setups. All types of insulation were studied for 316L samples. Only setup IV was studied

for the 8YSZ sample. This decision will be discussed later. A final height of 4 mm for all sintered samples was assumed.

*3.3 Materials and interaction properties*

The electrical resistivity, specific heat capacity and thermal conductivity of all setup components must be known for modeling. The data for graphite R7710 were taken from manufacturer. The electrical resistivity and thermal conductivity of stainless steel 316L were taken from the report by Ho and Chu (1977) and the specific heat was taken from the publication by Douglas and Victor (1961). The electrical resistivity of 8YSZ was taken from the work of Li et al. (2001) and thermal conductivity and specific heat from the paper by Vassen et al. (2000). The electrical resistivity, thermal conductivity and density of graphite felt and CFRC composite were taken from the supplier. The specific heat capacity of CFRC was calculated from its density and the specific heat of graphite. All these characteristics are displayed in Fig. 5 as a function of temperature.

The electric resistivity of steel 316L is much lower than the resistivity of graphite. Therefore, intensive current flow through the steel sample and heat generation in its volume can be expected. The electric resistivity of 8YSZ significantly decreases with increasing temperature. Nevertheless, the resistivity of 8YSZ always remains much higher than the resistivity of graphite. This means that current flows around the sample in the die, intensively heating its part adjacent to the sample. The electric resistivity of CFRC is only slightly higher than the resistivity of graphite. Therefore, CFRC spacers can be used without causing any problems. Another peculiarity of CFRC composite is a low thermal conductivity, which approaches the thermal conductivity of 8YSZ ceramic. Therefore, CFRC spacers can effectively insulate water-cooled electrodes from hot punches. It is also worth noting that the thermal conductivity of 316L steel is significantly lower than the thermal conductivity of graphite.

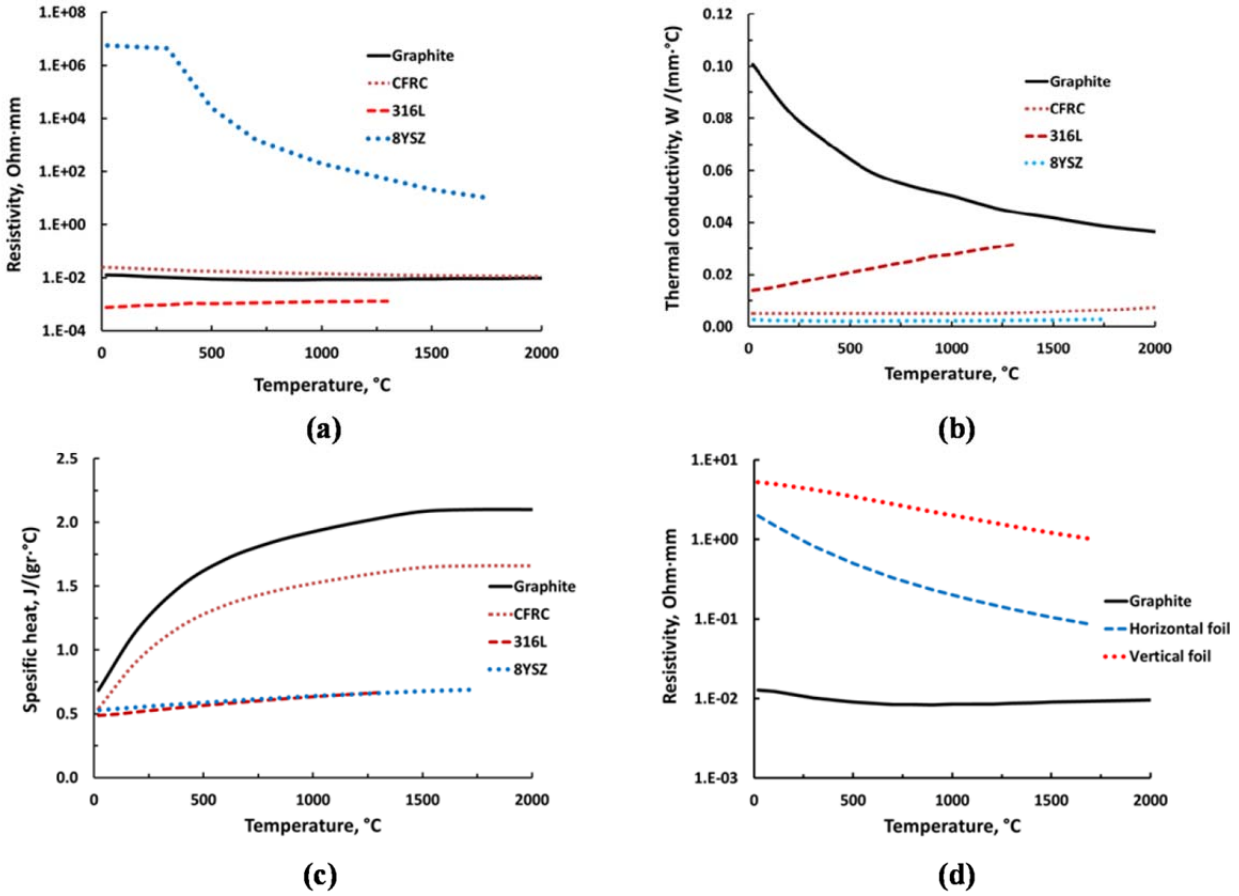


**Fig. 5.** Electrical and thermal properties of the tool, powder materials and foils.

Interaction properties include the emissivity coefficient of graphite, the convection coefficient relating to interaction between spacers and water-cooled electrodes and the electric and thermal resistivity of contacts between setup elements. The emissivity coefficient of graphite for surfaces radiating to ambient was taken as 0.8, corresponding to the recommendation of Zavaliangos at al. (2004). The emissivity coefficient within closed holes in the punches was assumed to be 0.945. The convection coefficient $h_c$ was determined by fitting the simulated temperature and the temperature measured by the thermocouple located in the upper spacer (Fig. 3b). A similar approach was applied by Achenani et al. (2017). The sintering cycle for 8YSZ sample with a diameter of 17 mm in setup I was used as reference. A good accuracy through the whole cycle was achieved with convection coefficient depending on temperature $T$. Here $T$ is an average of a cooled surface temperature $T_s$ and temperature of cooling water $T_w$ i.e. $T=(T_s+T_w)/2$. In our modeling the value of $T_w$=25.5°C was always used. In general, a convection coefficient depends on the performance of the

cooling system used and on the particular design of a FAST/SPS machine. In our case, the convection coefficient was specified by the linear function of temperature $h_c$=1800+7.9·$T$, W/(m$^2$·°C). With this approximation a reasonable agreement between calculated data and temperature measured with thermocouple during sintering in various setups was found. These results are summarized in Fig. 6. It is worth noticing that obtained convection coefficient is varied with temperature between 1800 W/(m$^2$·°C) and 2600 W/(m$^2$·°C). These values are consistent with the data reported by Achenani et al. (2017).

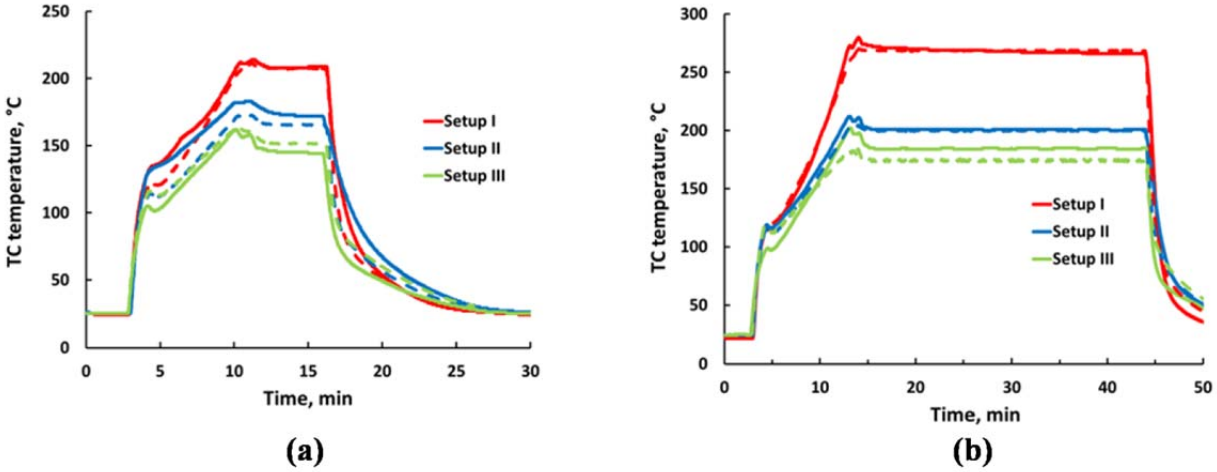


**Fig. 6.** Temperature measured with TC-1 (solid lines) and modeled with FEM (dashed lines): (a) – sintering of 316 samples; (b) – sintering of 8YSZ samples with a diameter of 17 mm.

The values of the electrical and thermal contact resistances were taken from the work of Vanmeensel et al. (2013). The effective resistivity of vertical and horizontal graphite foils (which includes both foil and contact resistances) was calculated by multiplying area specific contact resistivity and foil volume. The values obtained are compared with the electric resistivity of graphite in Fig. 5d. As evident from this figure, graphite foils have a much larger resistivity then bulk graphite. This is in agreement with Zavaliangos et al. (2004) and Manière et al. (2016), who also noticed a significant influence of contact resistances on current and temperature distribution within the FAST/SPS setup.

*3.4. Modeling procedure*

The ANSYS® 15.0 finite element software (ANSYS Inc., Canonsburg, USA) and PC with 3.2 GHz CPU and 128 GB RAM were used for FE modeling. The model was implemented as an input file written in the APDL language. One half of the setup was analyzed due to rotational symmetry. Despite the setup has also mirror symmetry, we did not use a quarter of configuration to avoid a possible inaccuracy in averaging between nodes in the plane of symmetry. The quadrilateral-shaped, axisymmetric PLANE 223 element with fully coupled thermal-electrical analysis capability was used. The element size of 0.5 mm for samples and of 2 mm for other setup components has been used. Contact interaction was modeled by TARGE169 and CONTA171 elements. The combination of free and mapped (where possible) meshing was used. The electric potential on the bottom of the lower spacer was taken as zero. A time-varying voltage was applied on the top of the upper spacer. This voltage was tuned by the proportional controller implemented in the APDL code to generate the predetermined time-temperature profile. The temperature calculated in the node at the bottom of the upper punch borehole (place of pyrometer reading) was fed back into the closed-loop algorithm. The input voltage was corrected by the voltage increment proportional to the difference between the calculated and predefined temperatures. The corrected voltage was limited by maximal and minimal preset values. The controller developed ensures good accuracy in virtual temperature regulation, as shown in Fig. 4. In the present paper, temperature calculation and subsequent voltage correction was performed twice a second. The modeling time for sintering of 316L powder in a fully insulated die (setup IV) with an internal diameter of 17.7 mm, 50.7 mm and 150.7 mm was about 30 min, 50 min and 1 h 30 min, respectively. The modeling of 8YSZ sintering in similar dies took more time. The modeling duration was about 1 h 20 min, 1 h 40 min and 2 h 20 min. Other cases of study required less time.

*3.5. Model verification*

Additional experiments were performed to verify used FEM model. The powders of 316L and 8YSZ were firstly sintered in a die with a diameter of 17.7 mm as described above. The die was not

insulated as in setup I. After sintering a borehole has been drilled in the middle of die wall until the drill tip touched the sintered sample. A K-type thermocouple has been inserted in this opening (TC-2 in Fig. 3). In such a way, the temperature of sample edge has been measured. The setup was heated-up in FAST/SPS device again. The heating cycle was as during sintering of 316L powder, i.e. with holding at temperature of 1100°C (Fig. 4a). The modeling of temperature field during such heat treatment of 316L and 8YSZ sample was carried out. The temperature development calculated for the samples edge and measured temperatures are compared in Fig. 7a,b. The modeling results match generally well the experimental data, particularly above 600°C.

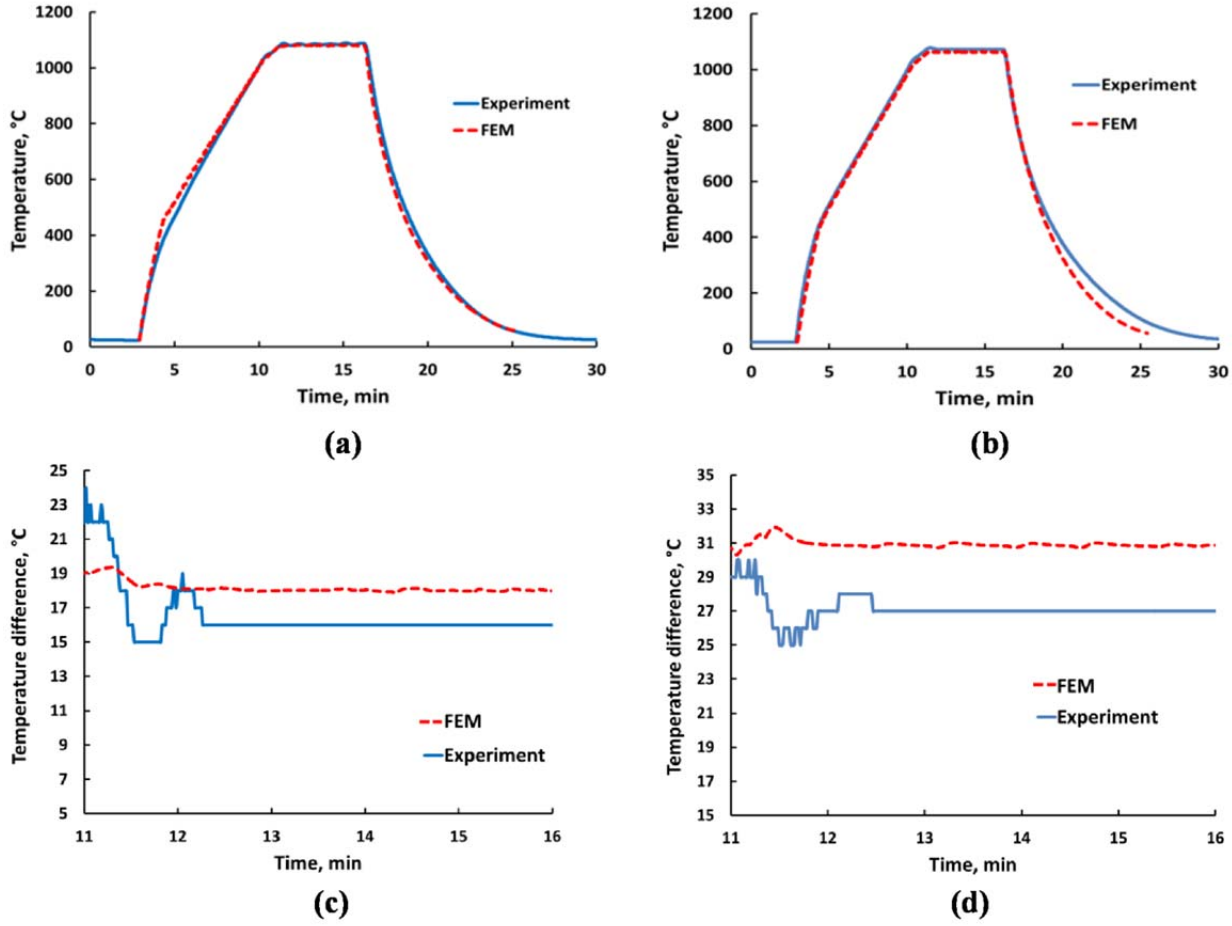


**Fig. 7.** Modeled and measured temperature during heating of 316L (left) and 8YSZ (right) samples with a diameter of 17 mm: (a), (b) – temperature development on the edge; (c), (d) – temperature difference between the center and edge during dwell at 1100°C.

difference between center and edge of 316L (left) and 8YSZ (right) samples with a diameter of 17 mm: (a), (b) – during entire cycle and (c), (d) – during dwell at 1100°C.

The temperature difference between samples center and their edge during holding stage was also evaluated. The theoretical values were directly calculated from modeling results. The experimental temperature drop was defined as a difference between pyrometer reading and temperature measured by thermocouple TC-2. A good agreement between calculated and experimental data was observed (Fig 7c,d). Thus, the applicability of presented model is confirmed at least for holding stage of sintering. The reliability of similar FAST/SPS models was also experimentally confirmed by phase (Räthel et al., 2009) and microstructure (Voisin et al., 2013) analysis, hardness (Vanmeensel et al., 2007) and grain size (Wolff et al., 2016) distribution and by direct temperature measurement at several points in the tool (Pavia et al., 2013).

# 4. Results and discussion

*4.1. Power consumption*

The development of power consumption during sintering in the small-sized die is shown in Fig. 8a for steel powder and in Fig. 9a for zirconia powder. In both cases, the power decreases sharply when the die wall is thermally insulated. The power is further reduced by thermally insulating the die faces. This effect is more pronounced for sintering of 8YSZ powder. Replacing the graphite spacers with CFRC spacers results in another strong decrease in power. The normalized power consumption during dwell stage in setups with different thermal insulation is summarized in Table 2. The power during sintering in a non-insulated setup I was taken as 100%.

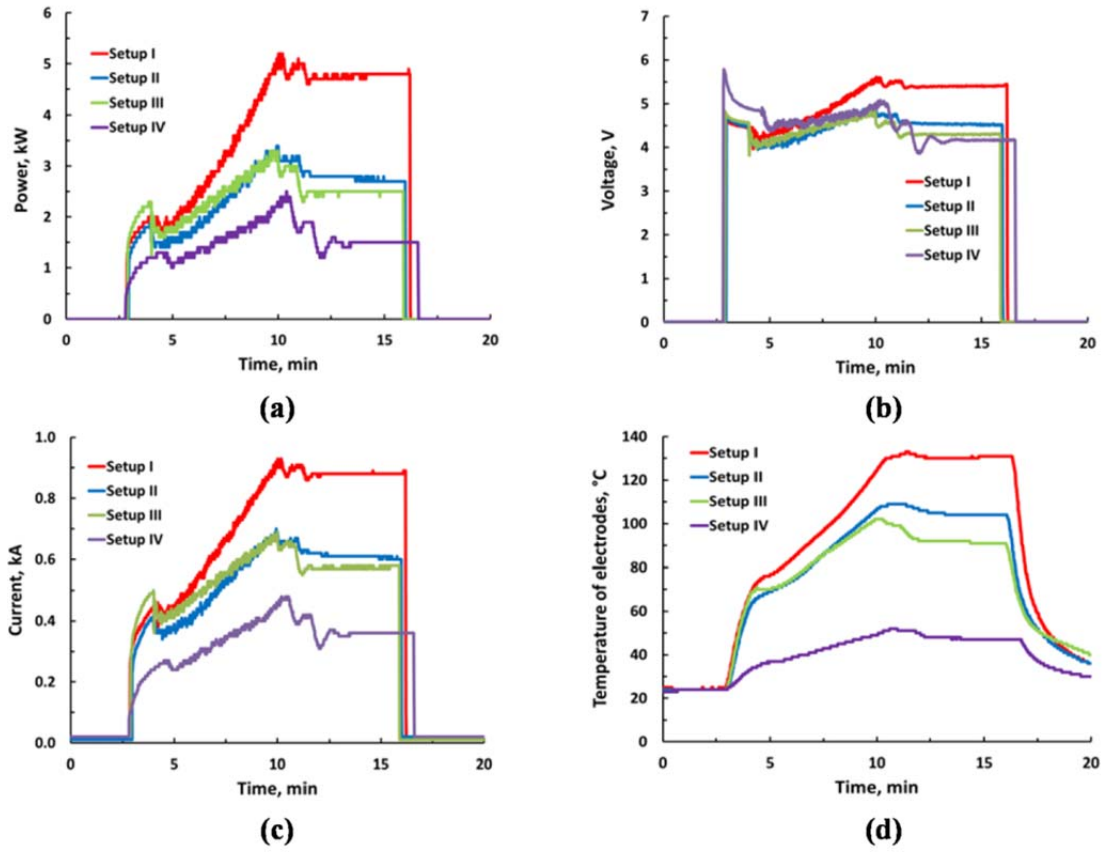


**Fig. 8.** Power, voltage, current and temperature of electrodes during sintering of 316L powder.

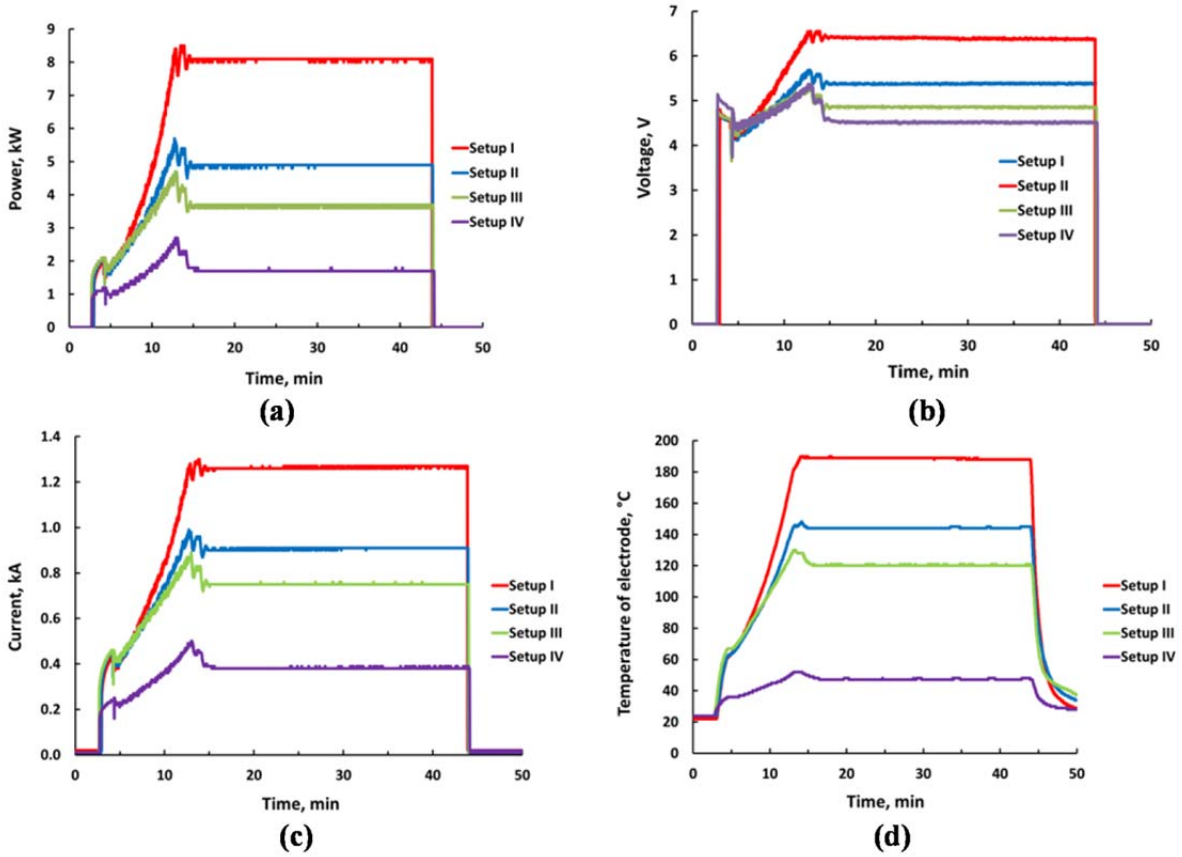


**Fig. 9.** Power, voltage, current and temperature of electrodes during sintering of 8YSZ powder.

**Table 2.**

Normalized power consumption during sintering dwell in setups with different insulation.

| *Powder* | *Setup I* | *Setup II* | *Setup III* | *Setup IV* |
|---|---|---|---|---|
| 316L | 100% | 57% | 51% | 31% |
| 8YSZ | 100% | 58% | 45% | 21% |

As evident from the table, the power consumed can be reduced nearly twice over when die insulation is used. Additional insulation of the FAST/SPS tool by replacing graphite spacers with CFRC spacers results in a threefold reduction in power for sintering of 316L powder and in a fivefold reduction for sintering of 8YSZ powder. Thus, the discussed methods of thermal insulation are very effective in decreasing energy consumption during sintering of both electrically conductive and non-conductive powders. Simultaneously, a certain reduction in voltage (Fig. 8b and Fig. 9b) and a significant decrease in current (Fig. 8c and Fig. 9c) were observed. Thermal insulation also substantially influences the temperature of the electrodes (Fig. 8d and Fig. 9d). This temperature can be reduced to the value of about 50°C when the die is fully insulated by graphite felt and CFRC spacers are used. This provides favorable operation conditions for electrodes and cooling system. It should be pointed out that we did not notice any essential influence of thermal insulation on the densification behavior of both powders. The application of thermal insulation slows cooling down. This effect is most pronounced when CFRC spacers are used (Fig. 4). Slow cooling can be a serious drawback in batch production. This problem can be solved by setup cooling outside the sintering chamber of the FAST/SPS machine. Such an approach is currently considered a promising route towards the industrial application of the FAST/SPS technique. Although, for many ceramics sensitive to thermal shock, slow cooling is desirable to avoid their fracture.

*4.2. Temperature distribution*

The influence of insulation on temperature distribution is another important consideration in FAST/SPS practice. This problem is studied in the present paper by the FEM modeling of steady-state temperature distribution during dwell. The calculated temperature contours for sintering in the

die with a diameter of 17.7 mm are presented in Fig. 10 for the 316L powder and in Fig. 11 for the 8YSZ powder. The use of thermal insulation and the application of CFRC spacers results in a remarkable homogenization of the temperature in sintered samples and in entire setups. The radial temperature gradient is most important for thin samples, such as in the present study. The temperature distribution in a radial central cross-section of the entire setup and in the samples with a diameter of 17 mm is shown in Fig. 12. The temperature decreases from the center of both 316L and 8YSZ samples to their edge. A sharp drop in the temperature upon contact between the sample and die is typical for the conductive 316L sample (Fig. 12a). A more smooth temperature transition is observed for the non-conductive 8YSZ sample (Fig. 12b). The temperature further decreases in the die wall. This temperature pattern is most pronounced for setup I without insulation. Finally, the intensive temperature decrease occurs in the insulating felt. The temperature on the external felt surface decreases to 445°C during sintering of 316L powder at 1100°C and to 525°C during sintering of 8YSZ powder at 1375°C. Thus, for all setups with die wall insulation, the heat loss due to radiation drastically decreases. This is the reason for the first drop in power observed in the experiments with the insulated die wall (setup II in Fig. 8 and Fig. 9). Insulation considerably influences the radial temperature gradient in both conductive and non-conductive samples, as shown in Fig. 12c and Fig.12d. During sintering in the non-insulated setup I, the difference between the temperature in the center and at the edge is 20°C for the 316L powder and 60°C for the 8YSZ powder. The difference in temperature decreases to 10°C for the 316L sample and to 16°C for the 8YSZ sample when die wall insulation in setup II is used. Such temperature gradients can be considered acceptable. An additional decrease in the temperature gradient can be achieved by insulating die faces as in setup III. In such a case, the temperature difference between the center and the edge diminishes to 5°C for the 316L sample and to 6°C for the 8YSZ sample. The replacing graphite spacers with CFRC spacers in setup IV leads to a temperature difference of 3°C for the 316L sample and 5°C for the 8YSZ sample. It is worth noticing that in the last case, the temperature in the sample center closely approaches its predefined value because of minimization in the axial

temperature gradient. Thus, during sintering of small conductive or non-conductive samples, the application of die wall insulation can be sufficient if only temperature homogeneity in a sample is desired. If energy consumption is also to be reduced, then full die insulation and the application of CRFC spacers can be recommended.

As expected, temperature gradients become larger during sintering of medium-sized samples with diameters of 50 mm (Fig. 13). The temperature drop from the sample center to the sample border reaches 67°C for 316L in a non-insulated die. The temperature distribution across its central cross-section has the same profile as was observed for the small-sized 316L sample. The temperature difference decreased to 38°C after die wall insulation. The additional insulation of die faces results in a further decrease in the temperature difference to 21°C. The use of CFRC spacers reduces the temperature drop to 13°C. Thus, during sintering of a medium-sized 316L sample, the insulation of die wall and die faces may be sufficient to reduce the temperature gradient to the acceptable value of 20°C. The situation is different when the non-conductive 8YSZ powder is sintered in a medium-sized die. In contrast to the sintering of 316L powder, the temperature mainly increases from the sample center towards its edge. This is the result of a particular current path and the current density distribution, as discussed below. However, the temperature decreases in the vicinity of non-insulated die wall in setup I. This is a consequence of the intensive heat loss caused by radiation from the die wall. In the present study, the difference between maximal and minimal temperature values for the 8YSZ medium-sized sample was around 40°C. The insulation of die wall decreases radiation and as a result significantly increases temperature inhomogeneity in setup II. The temperature difference reaches the value of 88°C. The additional insulation of die faces in setup III further decreases the heat loss. Therefore, larger temperature difference of 115°C was modeled for sintering in this setup. The negative effect of die insulation on temperature homogeneity for the sintering of medium-sized, non-conductive alumina samples was also reported by Muñoz and Anselmi-Tamburini (2013) and by Achenani et al. (2017). At the same time, the replacing of graphite spacers with CFRC protection plates in setup IV leads to a strong reduction in the

temperature difference of up to 20°C. Therefore, full insulation of medium-sized die in combination with the use of CFRC spacers could be a good solution for sintering non-conductive samples from both viewpoints: a reduction in energy consumption and a decrease in temperature gradients to admissive value.

Thermal heterogeneity continues to increase during sintering in the large-sized die (Fig. 14). The temperature pattern in the large-sized 316L sample is similar to the patterns modeled for the small-sized and the medium-sized steel samples. This pattern is determined by current density distribution and related heat generation along the horizontal faces of the 316L sample. The electrical resistivity of 316L steel is much lower than the resistivity of graphite (Fig. 5a). Therefore, current density varies from a maximum near the sample center to a minimum at the sample edge (Fig. 15a). The Joule's heat is generated mostly in the punch due to the higher resistivity of graphite compared to the resistivity of steel (Fig. 15b). In accordance with the current density profile, the intensity of heat generation varies from a maximum near the sample center to a minimum at its edge. The heat rapidly spreads from the punch to the sample owing to the high thermal conductivity of graphite. As a result, the temperature decreases from the sample center to the sample edge. The modeled temperature variances are summarized in Table 3. The temperature difference alters from 123°C for non-insulated die to 41°C for fully insulated die and CFRC spacers. The latter value is rather too large for sintering practice. It can be further reduced by optimizing setup design aiming to homogenize current density near the sample horizontal faces. For example, Voisin et al. (2013) reduced temperature non-uniformity in a conductive TiAl sample with a diameter of 100 mm from 125°C to 30°C by enlarging punch length and die height in combination with reduced spacer size. During sintering of non-conductive 8YSZ powder, whole current flows around the sample in the die, as shown in Fig. 15b. Heat generation is intense in the die portion adjacent to the sample edge. The quantity of heat is proportional to the total current, which increases with increasing sample and setup size. This leads to overheating of the sample edge. The temperature in the non-conductive sample correspondingly decreases from its edge to the center (Fig. 13b, 14b). Localized heat

generation can be fully compensated by energy loss due to radiation and water cooling of electrodes for sintering of the small-sized sample. In this case, the temperature diminishes from the sample center to the edge, as presented in Fig. 12b. During sintering of a non-conductive sample of medium size, edge overheating can be only partly counterbalanced by radiation heat loss in the non-insulated die. In this case, the temperature firstly increases from the center to the maximum and then diminishes towards the edge (Fig. 13b). The insulation of die wall and die faces suppresses radiation and the temperature continuously increases from the sample center to the sample edge. The application of CFRC spacers results in the radical reduction of current (Fig. 9c). The heat generation around the edge diminishes correspondingly. This leads to temperature homogenization and to an acceptable temperature gradient in the medium-sized sample (Fig. 13b). A huge current is required for sintering of the large-sized 8YSZ sample. Current density in the die portion adjacent to the sample edge is very large and heat concentration is enormous (Fig. 15d). This leads to fast overheating of the sample edge to sintering temperatures and above, while the sample center remains relatively cold. Thus, full densification of sample edge and poor sintering of sample center can be expected if traditional FAST/SPS tool design is used. This situation can be countered to some extent by the use of CFRC spacers, leading to a reduction in total current. Nevertheless, this measure does not provide fully acceptable temperature homogeneity in large samples, as shown in Fig. 14b and in Table 4. For successful manufacturing of non-conductive large-sized samples, tool design and sintering cycle must be optimized. This is the goal of our further work. Another possibility is adding an electrically conducive component to the basic non-conductive powder, making the sample electrically conductive, as proposed Vanmeensel et al. (2008). At this place, it should be pointed out that, the presented results should be considered rather as a guide to application of thermal insulation. The numerical values for temperature gradients can deviate from the data presented here. The reason for that is a complex influence of different accidental factors which is not possible to include into theoretical model. Particularly, Manière et al. (2016) emphasize a large influence of vertical contact resistance which could vary in a wide range.

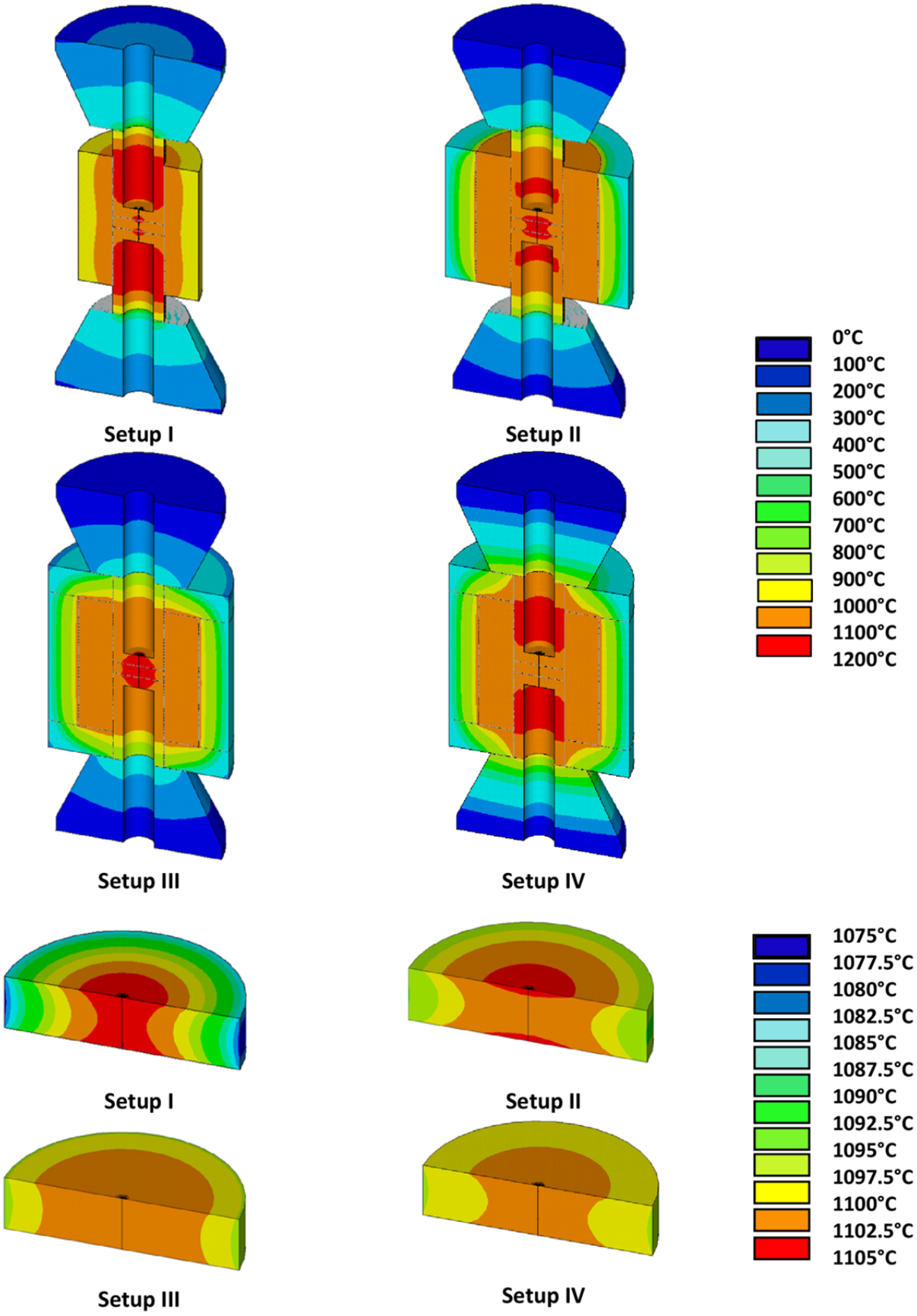


**Fig. 10.** Influence of insulation on the temperature distribution in the entire setup and in the 316L sample (diameter of 17.7 mm) during sintering dwell.

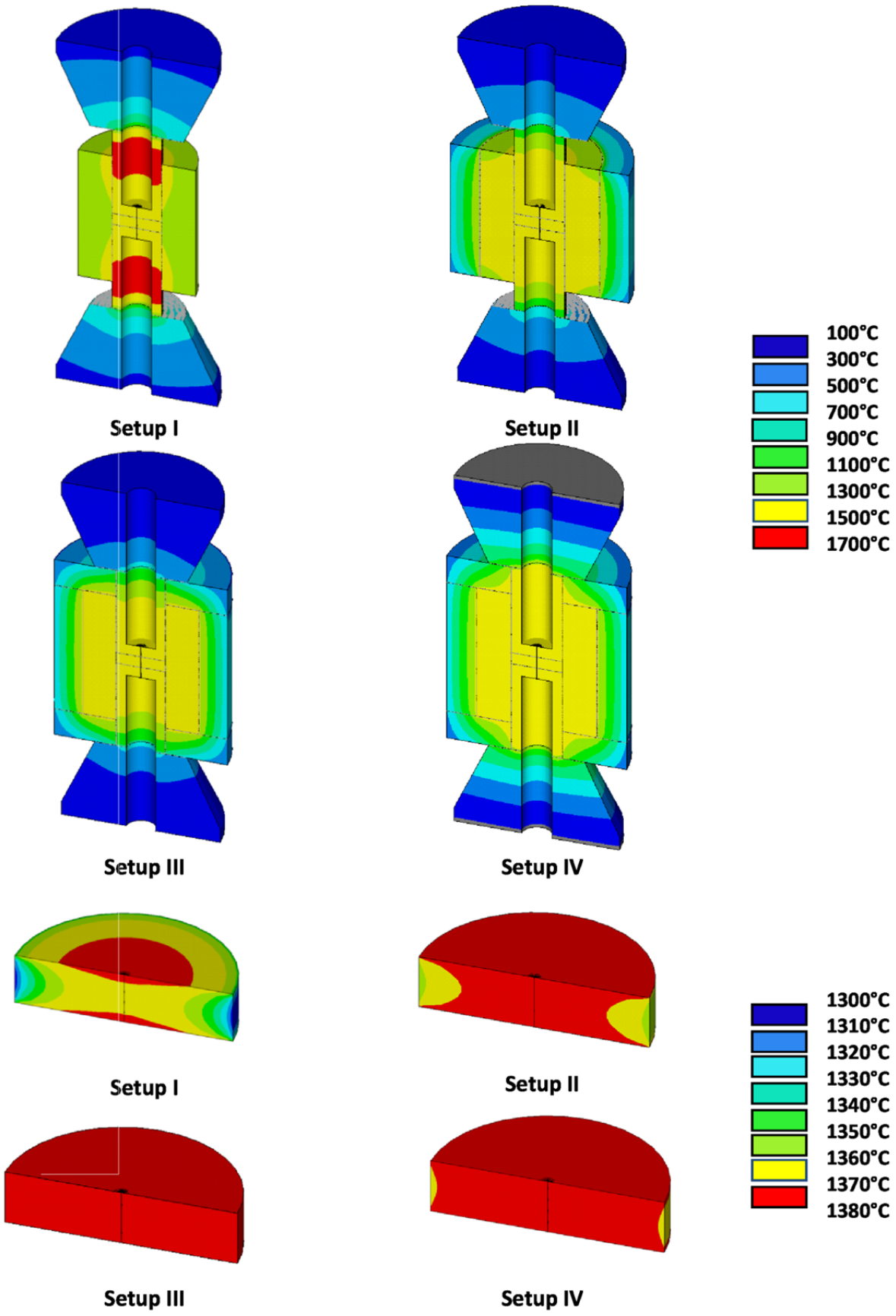


**Fig. 11.** Influence of insulation on the temperature distribution in the entire setup and in the 8YSZ sample (diameter of 17.7 mm) during sintering dwell.

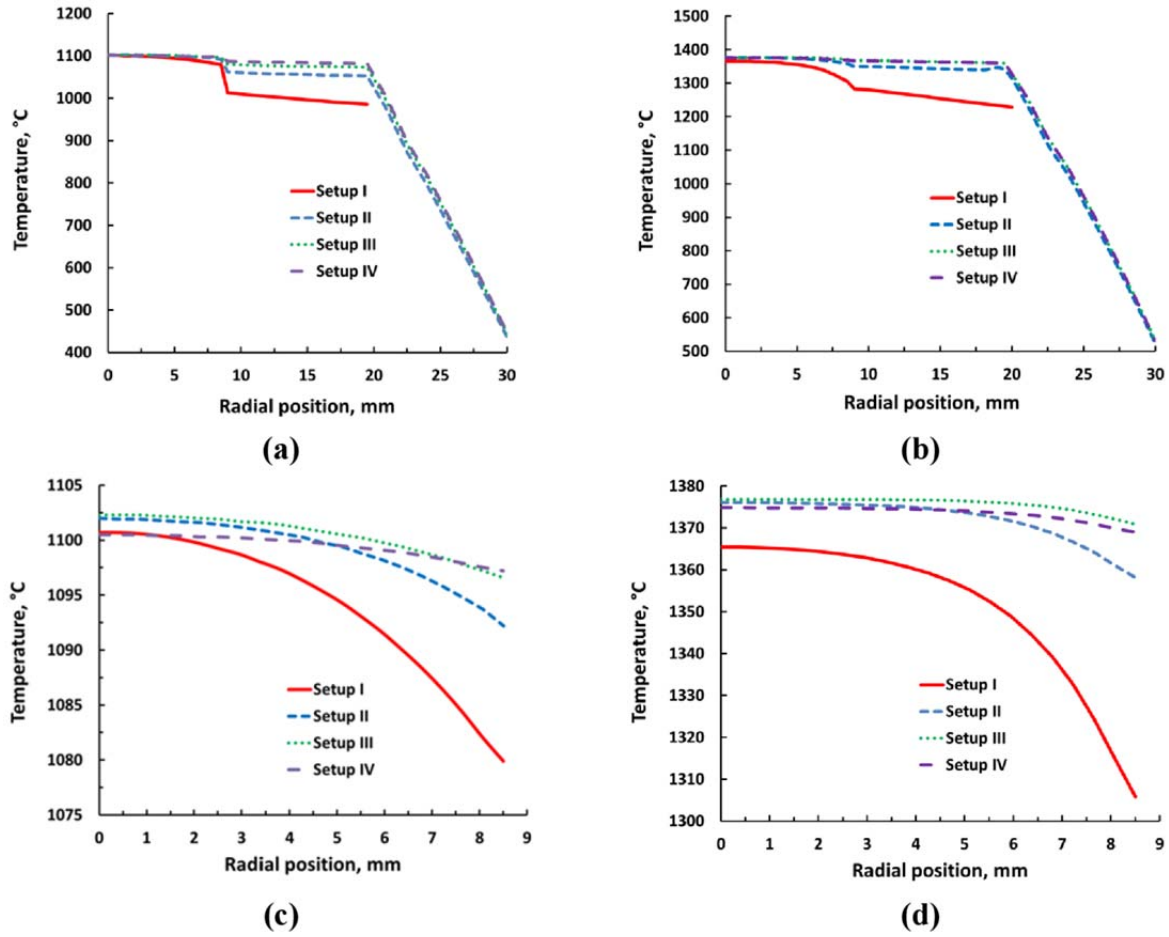


**Fig. 12.** Radial temperature distribution in the central cross-section: (a), (b) – entire setup; (c), (d) – sample (diameter of 17.7 mm). Left – 316L powder, right – 8YSZ powder.

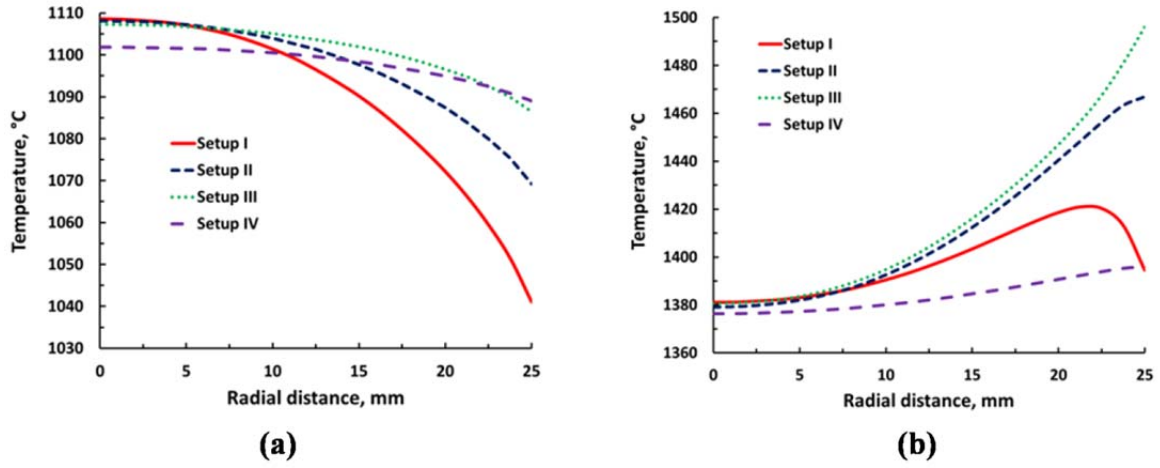


**Fig. 13.** Radial temperature distribution in the central cross-section of the medium-sized sample (diameter of 50 mm): (a) – 316L powder; (b) – 8YSZ powder.

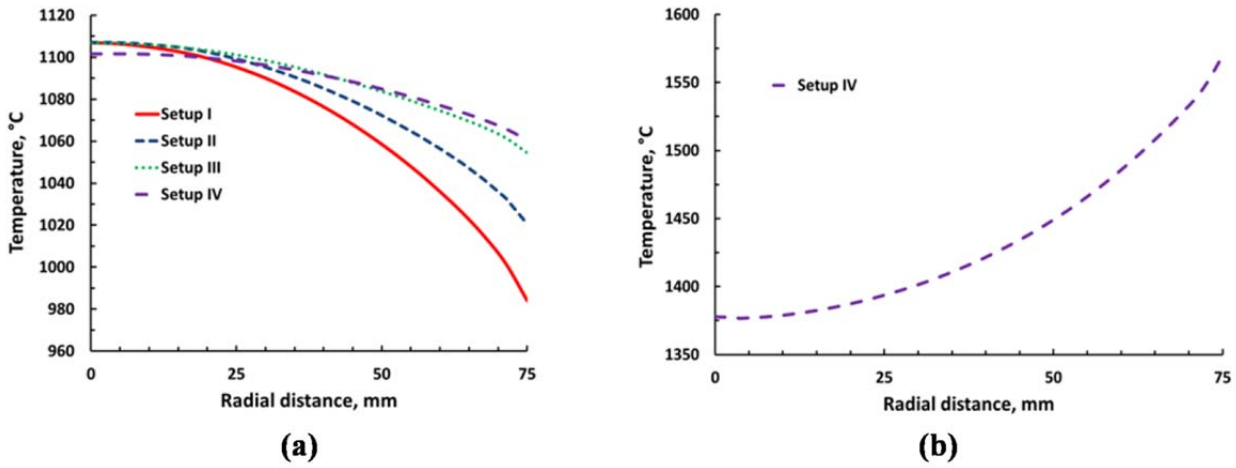


**Fig. 14.** Radial temperature distribution in the central cross-section of the large-sized sample (diameter of 150 mm): (a) – 316L powder; (b) – 8YSZ powder.

**Table 3.**

Maximal temperature difference during dwell stage of sintering of 316L powder in different dies.

| *Die* | *17.7 mm* | *50.7 mm* | *150.7 mm* |
|---|---|---|---|
| *Setup I* | 20 | 67 | 123 |
| *Setup II* | 10 | 38 | 87 |
| *Setup III* | 5 | 21 | 52 |
| *Setup IV* | 3 | 13 | 41 |

**Table 4.**

Maximal temperature difference during dwell stage of sintering of 8YSZ powder in different dies.

| *Die* | *17.7 mm* | *50.7 mm* | *150.7 mm* |
|---|---|---|---|
| *Setup I* | 60 | 40 | - |
| *Setup II* | 16 | 88 | - |
| *Setup III* | 6 | 115 | - |
| *Setup IV* | 5 | 20 | 197 |

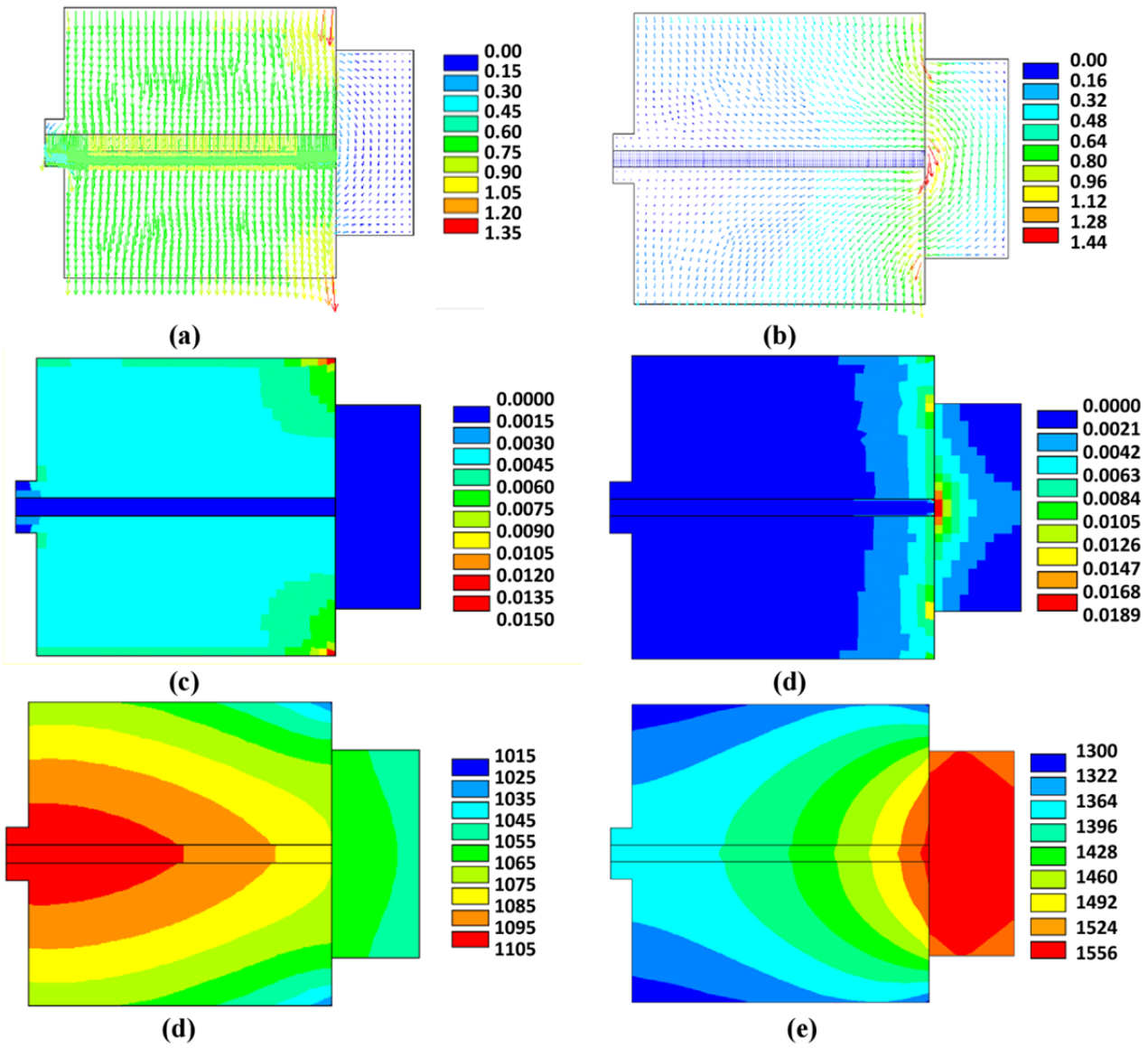


**Fig. 15.** Current density in A·mm$^{-2}$ (a) – (b), specific Joule's heat in W·mm$^{-3}$ (c) – (d) and temperature in °C (e) – (f) in large setup IV (sample diameter of 150 mm) for 316 powder (left) and for 8YSZ powder (right) during dwell at 1100°C and 1375°C, respectively.

## 5. Conclusions

- Thermal insulation is a simple and effective way of increasing the efficiency of the FAST/SPS technique, as it significantly diminishes energy consumption and in most cases homogenizes the temperature distribution within the sintered part. Insulating the die wall with graphite felt leads to a strong decrease in power demand during the sintering of both conductive and non-conductive powders. This effect is additionally enhanced by thermal insulation of the top and bottom die faces.

Power consumption during the dwell stage of a sintering cycle can be reduced more than twice over when full die insulation with graphite felt is used.

- Further energy decreases can be achieved by thermal insulation of the FAST/SPS tool from water-cooled electrodes. This can be done by replacing traditional graphite spacers with spacers manufactured from carbon fiber reinforced carbon composite with a much lower thermal conductivity. In this case, power consumption during dwell decreases three to five times over, depending on the sintering temperature.
- Advanced thermal insulation causes some decrease in voltage and a pronounced decrease in current during the FAST/SPS cycle. As a result, the temperature of the water-cooled electrodes drops to approximately 50°C, providing their beneficial working conditions. Thermal insulation does not significantly influence the densification of both conductive and non-conductive powders.
- Thermal insulation considerably influences the temperature homogeneity during FAST/SPS sintering. The degree of influence depends on the sintering temperature, sample size, powder conductivity and tool design. Thermal insulation of the die wall usually provides acceptable temperature homogeneity in small-sized (around 20 mm in diameter) samples independent of their conductivity.
- The influence of thermal insulation on temperature distribution becomes ambiguous during sintering of medium-sized (diameter of around 50 mm) samples and large-sized (diameter of around 150 mm) parts. The acceptable temperature homogeneity in medium-sized samples can only be achieved by supplementary insulation of die faces and the application of CFRC spacers. The optimization of tool design is additionally required before sintering large-sized conductive samples.
- Thermal insulation apparently cannot provide sufficient temperature homogeneity during sintering of non-conductive, large-sized parts. Here, additional optimization of current paths and minimization of current amount by implementing a special tool design and by tuning the sintering cycle are required.

# References

Achenani Y., Saâdaoui M., Cheddadi A., Bonnefont G., Fantozzi G., 2017. Finite element modeling of spark plasma sintering: Application to the reduction of temperature inhomogeneities, case of alumina. Mater. Des. 116, 504-514. https://doi.org/10.1016/j.matdes.2016.12.054

Douglas T.B., Victor A.C., 1961. Enthalpy and specific heat capacity of nine corrosion-resistant alloys at high temperatures. J. Res. Natl. Bur. Stand. C 65, 65-69. https://doi.org/10.6028/jres065C.007

Giuntini D., Olevsky E. A., Garcia-Cardona C., Maximenko A.L., Haines C.D., Martin D.G., Kapoor D., 2013. Localized overheating phenomena and optimization of spark-plasma sintering tooling design. Materials 6, 2612-2632. https://doi.org/10.3390/ma6072612

Giuntini D., Räthel J., Herrmann M., Michaelis A., Olevsky E.A., 2015. Advancement of tooling for spark plasma sintering. J. Am. Ceram. Soc. 98, 3529-3537. https://doi.org/10.1111/jace.13528

Ho C.Y., Chu T.K., 1977. Electrical resistivity and thermal conductivity of nine selected AISI stainless steels, CINDAS Report 45, AISI, Washington D.C., pp. 20-22.

Huang L., Qian M., Lu H., Sun Y., Wang L., Zou J., 2017. Reducing electric current and energy consumption of spark plasma sintering via punch configuration design. Ceram. Int. 43, 17225-17228. https://doi.org/10.1016/j.ceramint.2017.09.048

Li Y., Gong J., Tang Z., Xie Y., Zhang Z., 2001. Temperature-independent activation energy for ionic conduction of zirconia based solid electrolytes. Acta Phys.-Chim. Sin. 17, 792-796.

Manière C., Durand L., Brisson E., Desplats H., Carré P., Rogeon P., Estournè C., 2016. Contact resistances in spark plasma sintering: From in-situ and ex-situ determinations to an extended model for the scale up of the process. J. Eur. Ceram. Soc. 36, 741-748. http://dx.doi.org/10.1016/j.jeurceramsoc.2016.12.010

Muñoz S., Anselmi-Tamburini U., 2013. Parametric investigation of temperature distribution in field activated sintering apparatus. Int. J. Adv. Manuf. Technol. 65, 127–140. https://doi.org/ 10.1007/s00170-012-4155-7

Pavia A., Durand L., Ajustron F., Bley V., Chevallier G., Peigney A., Estournès C., 2013. Electro-thermal measurements and finite element method simulations of a spark plasma sintering device. J. Mater. Process. Technol. 213, 1327–1336. https:// doi.org/10.1016/j.jmatprotec.2013.02.003

Räthel J., Herrmann M., Beckert W., 2009. Temperature distribution for electrically conductive and non-conductive materials during Field Assisted Sintering (FAST). J. Eur. Ceram. Soc. 29, 1419-1425. https:// doi.org/10.1016/j.jeurceramsoc.2008.09.01

Vanherck T., Lobry J., Jean G., Gonon M., Cambier F., 2015. Spark plasma sintering: Homogenization of the compact temperature field for non-conductive materials. Int. J. Appl. Ceram. Technol. 12 [S2], E1-E12. https:// doi.org/10.1111/ijac.12187.

Vanmeensel K., Laptev A., Hennicke J., Vleugels J., Van der Biest O., 2005. Modelling of the temperature distribution during field assisted sintering. Acta Mater. 53, 4379-4388. https:// doi.org/10.1016/j.actamat.2005.05.042

Vanmeensel K., Laptev A., Hennicke J., Vleugels J., Van der Biest O., 2007. The influence of percolation during pulsed electric current sintering of $ZrO_2$-TiN powder compacts with varying TiN content. Acta Mater. 55, 1801-1811. https:// doi.org/10.1016/j.actamat.2006.10.042

Vanmeensel K., Huang S.G., Laptev A., Salehi S.A., Swarnakar A.K., Van der Biest O., Vleugels J., 2008. Pulsed electric current sintering of electrically conductive ceramics. J. Mater. Sci. 43, 6435-6440. https:// doi.org/10.1007/s10853-008-2631-0

Vanmeensel K., Laptev A., Sheng H., Tkachenko I., Van der Biest O., Vleugels J., 2013. Experimental study and simulation of plastic deformation of zirconia-based ceramics in a pulsed electric current apparatus. Acta Mater. 61, 2376-2389. https://doi.org/10.1016/j.actamat.2013.01.008

Vassen R., Cao X., Tietz F., Basu D., Stöver D., 2000. Zirconates as new materials for thermal barrier coatings. J. Am. Ceram. Soc. 83, 2023-2028. https:// doi.org/10.1111/j.1151-2916.2000.tb01506.x

Voisin T., Durand L., Karnatak N., Le Gallet S., Thomas M., Le Berre Y., Castagné J-F., Coureta A., 2013. Temperature control during Spark Plasma Sintering and application to up-scaling and complex shaping. J. Mater. Process. Technol. 213, 269–278. https:// doi.org/10.1016/j.jmatprotec.2012.09.023

Wolff C., Mercier S., Couque H., Molinari A., Bernard F., Naimi F., 2016. Thermal-electrical-mechanical simulation of the nickel densification by Spark Plasma Sintering. Comparison with experiments. Mech. Mater.100, 126-147. https:// doi.org/10.1016/j.mechmat.2016.06.012

Zavaliangos A., Zhang J., Krammer M., Groza J.R., 2004. Temperature evolution during field activated sintering. Mater. Sci. Eng. A 379, 218-228. https:// doi.org/10.1016/j.msea.2004.01.052

**This research did not receive any special grant from founding agencies in the public, commercial or non-for-profit sectors.**